# Axisymmetric Interchange Calculations with NIMROD

**January 9, 2007**

Carl R. Sovinec

University of Wisconsin-Madison
Department of Engineering Physics



This work is supported by DOE grant DE-FC02-02ER54668.

**Abstract**

Axisymmetric interchange instabilities in ideal magnetohydrodynamics are considered for a code verification exercise. Linearized equations are solved for cylindrical equilibria with uniform axial current density and uniform axial magnetic field. Analytical results are obtained from eigenmode analysis, and different NIMROD computations are performed with the plane of finite elements representing either the $r$-$z$ plane or the $r$-$\theta$ plane of the periodic cylinder. Accuracy is confirmed for interchange without axial magnetic field with both representations and with the $r$-$z$ mesh for the large-axial-field case. No-slip conditions, which reduce the growth rate by 5.5%, are required with large-axial field and the $r$-$\theta$ mesh to avoid a numerical error. Possible improvements to the NIMROD representation are discussed.

## 1. Introduction

At nearly eleven years into the NIMROD project (http://nimrodteam.org), the code has been well exercised on many applications and test problems, only some of which have been documented. When the code converges, we have confidence that it provides accurate results for the specified parameters. Nonetheless, there are computations where we have to modify parameters, usually increasing diffusivities, in order to achieve convergence. The difficulties typically appear as high-wavenumber modes that grow rapidly. However, in linear computations of edge-localized modes (ELMs) with low values of electrical resistivity, we observe slow convergence properties and an unphysical dependence on the diffusivity for controlling magnetic divergence error. Convergence on ELMs is achieved at increased values of resistivity, but the value is not realistic for large tokamaks, and high-order polynomials (degree 5 and larger) are still required. It is also worth noting where the code works extremely well. At low pressure, even very slow magnetic reconnection processes are reproduced accurately. Tearing modes tend to be low wavenumber, but very localized features exist near the reconnection region. In addition, the project changed the standard for resolving anisotropy in MHD computations without mesh alignment.

The challenges associated with interchange behavior have received significant attention in the numerical literature. The book by Gruber and Rappaz [1] provides an extensive treatment of ideal MHD eigenvalue computations with finite elements. It emphasizes the 'non-standard' or singular nature of ideal MHD computations—when viewed as Sturm-Liouville problems—that results from resonant surfaces. In addition, stiffness in the time-dependent MHD system manifests itself as spectral sensitivity to point-wise numerical errors associated with compression in some finite element representations, leading to spectral pollution where a new unresolved mode appears as each new element is added. Degtyarev and Medvedev review a number of possible approaches to eigenvalue computations [2] and discuss advantages and disadvantages to the "hybrid finite elements" proposed in Ref. [1]. In the paper on NIMROD's MHD algorithm [3], we noted that time-dependent computations have flexibilities that are not available to eigenvalue computations, namely regularization via decreasing time-step. However, they typically solve higher-order differential systems due to resistivity, thermal conduction, two-fluid Ohm's law, etc. that preclude representations used for ideal MHD eigenvalue computations, at least for conforming representations. Nonetheless, the extremes of high-temperature plasmas can make ideal effects dominate everywhere except near resonant surfaces, and Lütjens and Luciani adopt a special treatment for the magnetic field to reproduce interchange thresholds accurately [4] in time-dependent XTOR computations. Expanding potentials instead of primitive fields can be used to separate shear and compressive flows analytically, e.g. the M3D code [5]

uses this formulation, but this approach increases the order of the differential system, and an order of accuracy is lost when taking spatial derivatives [6] to obtain the physical fields.

To assess where improvements can be made in NIMROD's spatial representation, we consider relatively simple linear ideal MHD problems in cylindrical geometry. We start with a pure *z*-pinch configuration without axial guide field. The equilibrium is unstable to the ideal MHD m=0 'sausage' instability with a close-fitting shell. Time-dependent computations are performed with the NIMROD code in two ways. First, the plane of two-dimensional finite elements is used to represent the *r*-*z* plane of a periodic cylinder using only the axisymmetric Fourier component for the azimuthal direction. Second, the finite elements are used to represent the $r$-$\theta$ plane with a single nonzero Fourier wavenumber for the axial direction. The NIMROD results are verified with a growth rate obtained from an ODE eigenvalue calculation. We also consider adding uniform axial magnetic field to the equilibrium, where the axial field is sufficiently large to make an axisymmetric mode nearly stable. The mode then has low wavenumber and may not be considered a true interchange mode, but NIMROD computations with a polar mesh show familiar difficulties with free-slip boundary conditions. In the equilibrium without axial field, the axisymmetric mode is resonant ($\mathbf{k}\cdot\mathbf{B}_0 = 0$) at all radii. With the guide field, the axisymmetric mode is not resonant. Future work will consider m≠0 modes that have an isolated resonant surface and are near the stability threshold, which is expected to be the most challenging case for interchange. What is described here is just a start on this interchange verification and code refinement effort.

The second section of this report describes the pinch equilibria and eigenvalue computations. The third section describes the NIMROD computations and comparisons with the eigenvalue results. The fourth section draws conclusions based on the interchange verifications performed so far. The appendix provides the input parameters for four of the NIMROD computations.

## 2. Equilibrium and Linear System

The equilibrium used in the test cases described here is very simple. The axial current density is uniform, so the azimuthal magnetic field varies linearly with radius, and the axial magnetic field is uniform. With the magnetic field normalized by its azimuthal component at the outer radius ($a$) of the cylinder, $B_a \equiv B_\theta(a)$, its azimuthal component is equivalent to the normalized radius, $x=r/a$,

$$\frac{B_\theta(r)}{B_a} = x \quad ,$$

and the axial component is equivalent to the normalized pitch ($\Phi$)

$$\frac{rB_z}{aB_\theta} = \frac{B_z}{B_a} = \Phi \quad .$$

We may also write the equilibrium pressure as an $x$-dependent normalized beta as

$$\frac{2\mu_0 P(x)}{B_a^2} = \beta - 2x^2 \quad ,$$

where the parameter $\beta$ is analogous to the poloidal beta on axis. Note that we must have $\beta \geq 2$. For convenience, the equilibrium mass density ($\rho$) is uniform, so the pressure profile represents a temperature profile.

When constructing the system for linear perturbations, we use the displacement vector $\underline{\xi}$, which is already normalized by *a*. With the ideal MHD Ohm's law and restricting to axisymmetric modes, the normalized perturbed magnetic field and pressure are

$$\mathbf{b} = \Phi \frac{\partial \underline{\xi}}{\partial z} - \left(x\hat{\theta} + \Phi\hat{z}\right)\nabla \cdot \underline{\xi} \tag{1}$$

$$p = 4x\xi_x - \gamma\left(\beta - 2x^2\right)\nabla \cdot \underline{\xi} \quad , \tag{2}$$

where $\gamma$ is the ratio of specific heats, and the axial coordinate and gradient operator are already normalized by *a*. From this point, we assume that perturbed fields oscillate in *z* and grow in time, for example $p(x,z,t) \rightarrow p(x)e^{\Gamma t + ikz}$, where *k* is the axial wavenumber multiplied by *a*. It is also convenient to define time in units of the Alfvén time $\tau_a = a\sqrt{\mu_0 \rho}\,/B_a$, so that Γ is the growth rate multiplied by $\tau_a$. Using the prime symbol to denote derivatives with respect to *x*, the linear system of equations is

$$b_x = ik\Phi\xi_x \tag{3a}$$

$$b_\theta = ik\left(\Phi\xi_\theta - x\xi_z\right) - \left(x\xi_x\right)' \tag{3b}$$

$$b_z = -\frac{\Phi}{x}\left(x\xi_x\right)' \tag{3c}$$

$$p = 4x\xi_x - \gamma\left(\beta - 2x^2\right)\left[\frac{1}{x}\left(x\xi_x\right)' + ik\xi_z\right] \tag{3d}$$

$$\Gamma^2\xi_x = ik\Phi b_x - 2b_\theta - \left(xb_\theta + \Phi b_z\right)' - \frac{1}{2}p' \tag{3e}$$

$$\Gamma^2\xi_\theta = 2b_x + ikb_\theta \tag{3f}$$

$$\Gamma^2\xi_z = -ikxb_\theta - \frac{ik}{2}p \quad . \tag{3g}$$

The factor of ½ appearing in the pressure-gradient terms arises from the normalization used for pressure.

The Φ=0 limit simplifies the linear system considerably. Perturbed magnetic field is in the azimuthal direction, and it arises from compressive motions only. The perturbed displacement vector lies in the *r*-*z* plane, and the entire system can be written in terms of $\xi_x$ and $b_\theta$. Further limiting consideration to incompressible motion leads to electrostatic fluid behavior, and the linear system

$$x^2\xi_x'' + x\xi_x' - \left(k^2x^2 + 1\right)\xi_x = 0$$

is essentially a modified Bessel's differential equation. Solutions that satisfy regularity at $x$=0 cannot satisfy zero normal displacement at $x$=1, so the incompressible limit is not unstable in the presence of a close-fitting wall. This does not rule-out instability when the plasma column is surrounded by a vacuum region.

When the equilibrium has an axial guide field, perturbations excite field-line bending, so the perturbed magnetic field at each $x$-value is not simply proportional to the divergence of displacement. A first-order system of equations that is suitable for ODE solvers is

$$\xi_x{}' = f - \frac{\xi_x}{x} \tag{4a}$$

$$\left(\mathrm{A}\Phi^2 + \mathrm{B}\Gamma^2\right) f' = \left[ \mathrm{A}\left(\Gamma^2 + k^2\Phi^2\right) - 4k^2\mathrm{X} - \frac{2x\Gamma^4\mathrm{A}'}{\mathrm{A}} \right] \xi_x - \frac{\Gamma^4\mathrm{B}'}{\mathrm{A}}\left(\Gamma^2 + k^2\Phi^2\right) f \tag{4b}$$

where

$$\mathrm{A} \equiv \Gamma^2\left(\Gamma^2 + k^2\Phi^2\right) + k^2\mathrm{B} \tag{5a}$$

$$\mathrm{B} \equiv \Gamma^2 x^2 + \gamma\left(\frac{\beta}{2} - x^2\right)\left(\Gamma^2 + k^2\Phi^2\right) \tag{5b}$$

$$\mathrm{X} \equiv \Gamma^2\left(x^2 + \Phi^2\right) + \gamma\, k^2\Phi^2\left(\frac{\beta}{2} - x^2\right) \quad . \tag{5c}$$

The system is equivalent to the Hain-Lüst equation [7,8] when it is simplified for axisymmetric perturbations and uniform current density.

Mathematical regularity for axisymmetric modes requires $\xi_x = 0$ at $x$=0; however, $f \equiv x^{-1}(x\xi_x)'$ may be nonzero. Discrete modes are found by integrating from $x$=0 to $x$=1 with different values of $\Gamma^2$ for a given $k$-value and identifying the solutions that satisfy $\xi_x(1) = 0$ as eigenmodes. Eigenmodes with negative values of $\Gamma^2$ are stable modes. Besides the discrete modes, where Eqs. (4a-b) lead to standard Sturm-Liouville problems, there is also singular behavior. The coefficient of $f'$ on the left side of (4b) has a zero if $\Gamma^2 = -k^2\Phi^2$; this mode is a global torsional Alfvén wave. In addition, the coefficient is zero for a range of eigenvalues that satisfy

$$\Gamma^2 = -\frac{\gamma\left(\frac{\beta}{2} - x^2\right)k^2\Phi^2}{x^2 + \Phi^2 + \gamma\left(\frac{\beta}{2} - x^2\right)} \tag{6}$$

with $0 \le x \le 1$. This is the sound continuum with singular behavior at the location where (6) is satisfied. Finding the eigenfunction from ODE computations requires a second integration from

$x$=1 inward to the location of the singularity. Our present verification effort is focused on unstable axisymmetric modes, which are not singular and may be treated as standard Sturm-Liouville problems. In addition, the perturbed velocity and displacement vector profiles are related by the parameter Γ, so we may compare velocity profiles from linear initial-value (NIMROD) computations with the displacement profiles from eigenmode analysis.

**3. Verification Calculations**

We have performed two sets of verification calculations. The first does not have an axial guide-field, and the second has a guide field that is large enough to bring the unstable mode near the threshold of stability. All of the calculations have the minimum value of two for the parameter $\beta$, and the ratio of specific heats is 5/3. Time-dependent computations are performed with the $r$-$z$ mesh and the $r$-$\theta$ mesh for both parameter sets.

3.1. Limit of Φ=0

When the equilibrium does not have a guide-field, axisymmetric perturbations are unstable and have large growth rates when $|k|$ is large. Results of eigenmode computations for the fastest-growing mode as a function of $k$ are shown in Fig. 1. The corresponding eigenfunctions have one node in $x$, and time-dependent computations for a single $k$-value eventually show just this mode. Other unstable modes have more than one node in $x$, but their growth rates are smaller.

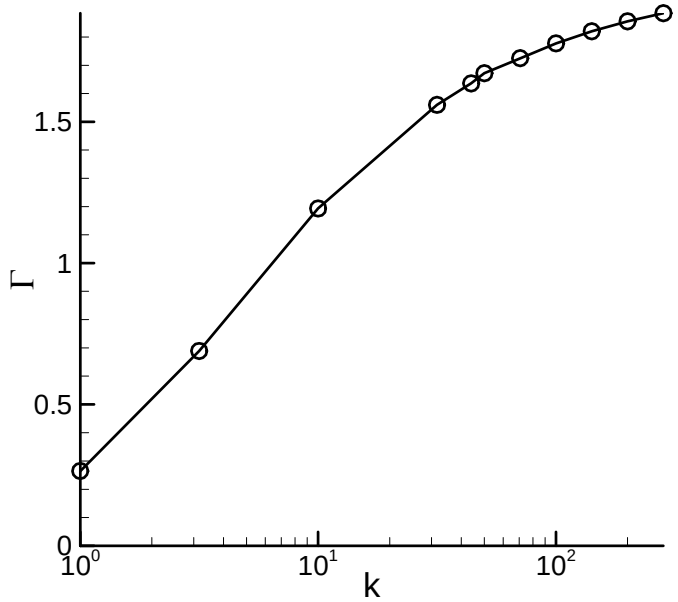


Figure 1. Eigenmode results on normalized maximum growth-rate as axial wavenumber is varied for the Φ=0 limit.

For NIMROD computations with an $r$-$\theta$ mesh, we select the $k$-value when setting the Fourier component index and the length of the periodic cylinder. However, computations with an $r$-$z$ mesh (and the Fourier index set to zero for the azimuthal direction) allow multiple $k$-values. For example, a set of computations with a 12×24 (radial×axial) mesh of bicubic elements with

$0 \le z \le \pi/11$ allows $k$-values approximately as large as 800. A sinusoidal perturbation with two wavelengths in the axial direction is sufficiently close to the asymptotic range that only the $k$=44 mode appears in the result. Temporal convergence information for NIMROD computations of this mode without viscosity and resistivity is shown in Fig. 2. Clearly, the agreement with the eigenvalue computation is good for this relatively simple interchange behavior, but two points are worth noting. First, NIMROD uses free-slip conditions on velocity when there is no viscosity. Though this often causes numerical difficulties (as we shall see below), they do not arise with this rapidly growing mode.[1] Second, the semi-implicit advance with the linear ideal-MHD force operator (Fig. 2a and see Ref. 3 for more information) gives excellent accuracy for the ideal mode with $\Gamma \Delta t > 0.1$. This is not surprising for this case, since the semi-implicit operator represents all of the relevant dynamics. Simplifying the semi-operator to the Laplacian requires smaller time-steps (Fig. 2b), but these computations also converge.

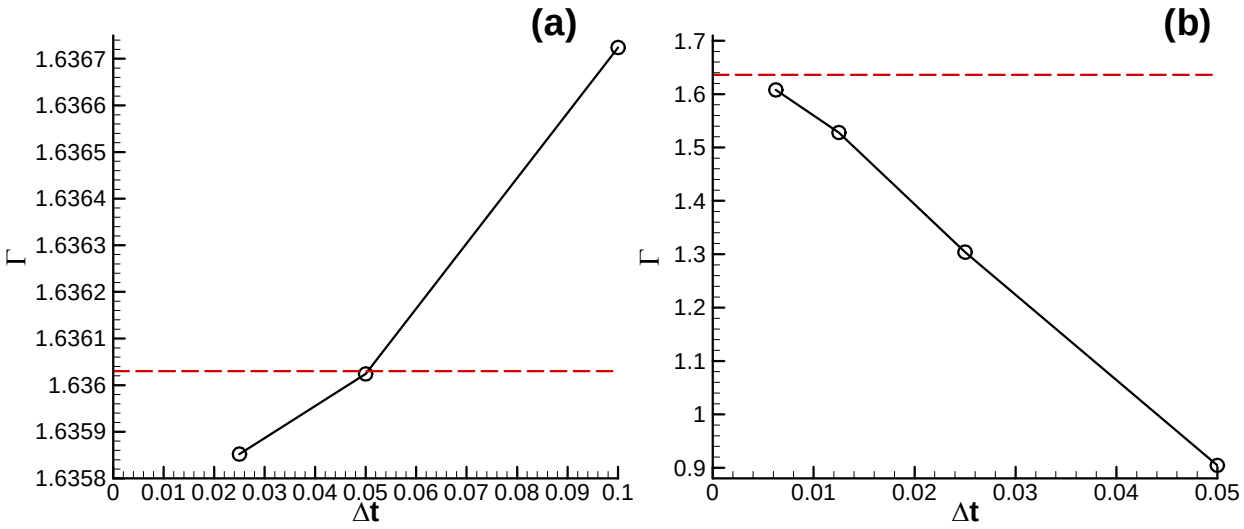


Figure 2. Temporal convergence for NIMROD computations of the $k$=44, $\Phi$=0 mode for the 12×24 mesh of bicubic elements for the $r$-$z$ plane. Results obtained using the linear ideal-MHD force operator for the semi-implicit operator are shown in (a), and results obtained with the Laplacian operator are shown in (b); note the different axis scales. The dashed lines show the eigenmode result, and $\Delta t$ is relative to $\tau_a$.

NIMROD computations with a 12×24 (radial×azimuthal) mesh of curved bicubic elements for the $r$-$\theta$ plane achieve similar results. With $\Delta t$=0.05, the computed growth-rate is 1.6356, and the eigenmode has no appreciable azimuthal variation.

Returning to the $r$-$z$ mesh, we observe that an unresolved mode can appear as growing numerical noise. With the 12×24 (radial×axial) mesh covering $0 \le z \le \pi/11$, the two-wavelength initial perturbation excites just the $k$=44 mode, and the NIMROD eigenfunction matches the result of the eigenmode analysis (Figs 3a-b). However, with the same mesh covering $0 \le z \le 6\pi$, the largest $k$-value on the mesh is approximately 12, which is not in the asymptotic range. Figure

[1] This mode is not near the incompressible limit. The eigenmode analysis shows that when $\gamma$ is increased from 5/3 to 100, the growth rate decreases by 65%.

3c shows the radial component of velocity resulting from multiple long-wavelength perturbations. The growth-rate diagnostic indicates 1.04, but the value slowly drifts in time as unresolved perturbations compete.

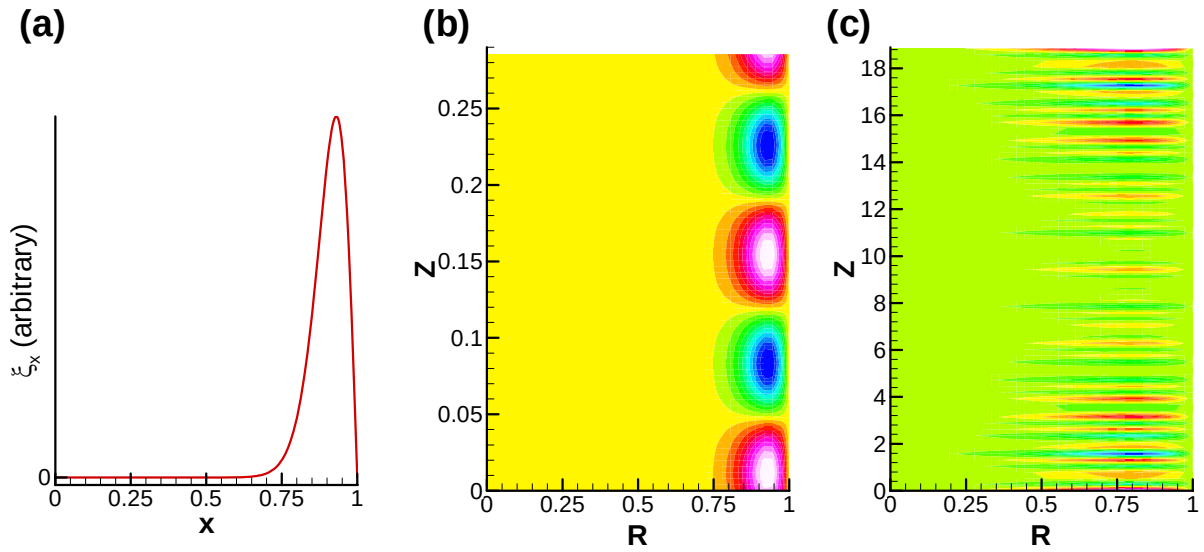


Figure 3. Radial displacement for the $k$=44, $\Phi$=0 mode from eigenmode analysis (a) and contours of the radial component of velocity for the resolved $k$=44 NIMROD computation (b) and a NIMROD computation with inadequate axial resolution (c).

3.2. Equilibria with Guide Field

When an axial guide field is added to the equilibrium, axisymmetric perturbations cannot exchange flux tubes from different radii without bending them. The resulting restoring force reduces the growth rate and broadens the eigenfunction. If the guide field is sufficiently large, it stabilizes the axisymmetric mode. For large $k$-values, very little guide field is required for stabilization. For $k$=10, for example, the mode is unstable with $\Phi$=0.1 but stable with $\Phi$=0.2. Here, we consider $k$=0.25, where adding the guide field initially has a slightly destabilizing effect according to our eigenmode analysis (Fig. 4).

Using the $k$=0.25, $\Phi$=0.5 mode for the comparison, an inviscid NIMROD calculation with a 12×12 (radial×axial) mesh of bicubic elements finds $\Gamma$=0.02571 with $\Delta t$=2.5 (Alfvén times), and the eigenmode analysis finds the mode at $\Gamma$=0.02570. Other computations show that these relatively slow instabilities are more sensitive to the coefficients chosen for the semi-implicit operator,[2] but accuracy is also good at large values of $\Delta t$. With $\Delta t$=10, $\Gamma$=0.02584, i.e. less than 1% error with only four time-steps per growth-time. The eigenfunctions from the NIMROD computation and from the eigenmode analysis are compared in Fig. 5.

When the same inviscid calculation (with free-slip boundary conditions) is attempted with polar $r$-$\theta$ meshes, the physical mode is lost in a fast unphysical mode at the boundary. With an 8×24 (radial×azimuthal) mesh of curved biquartic elements and $\Delta t$=2.5, the numerical instability

[2] Setting the NIMROD parameters si_fac_mhd and si_fac_pres to 1.5 instead of 1 reduces the growth rate of a $k$=1 computation by 8.7%.

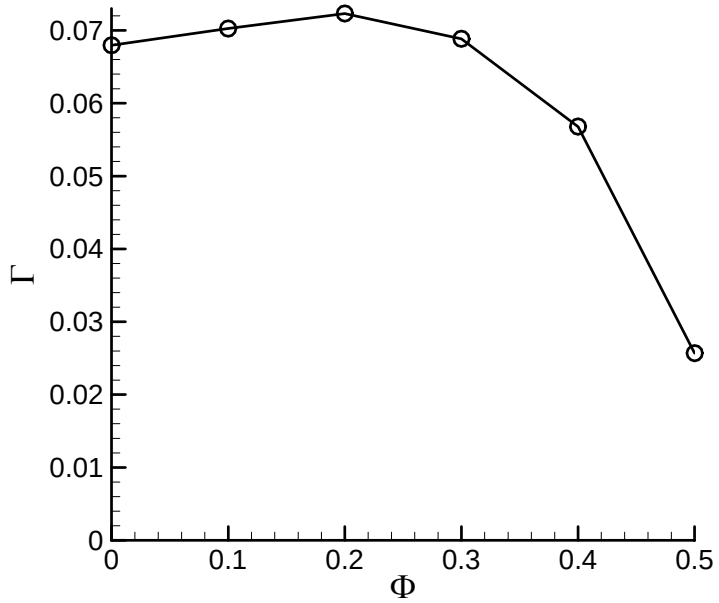


Figure 4. Eigenmode results on normalized maximum growth-rate as pitch (Φ) is varied for the $k$=0.25 axisymmetric mode. The stability threshold occurs at Φ<0.6.

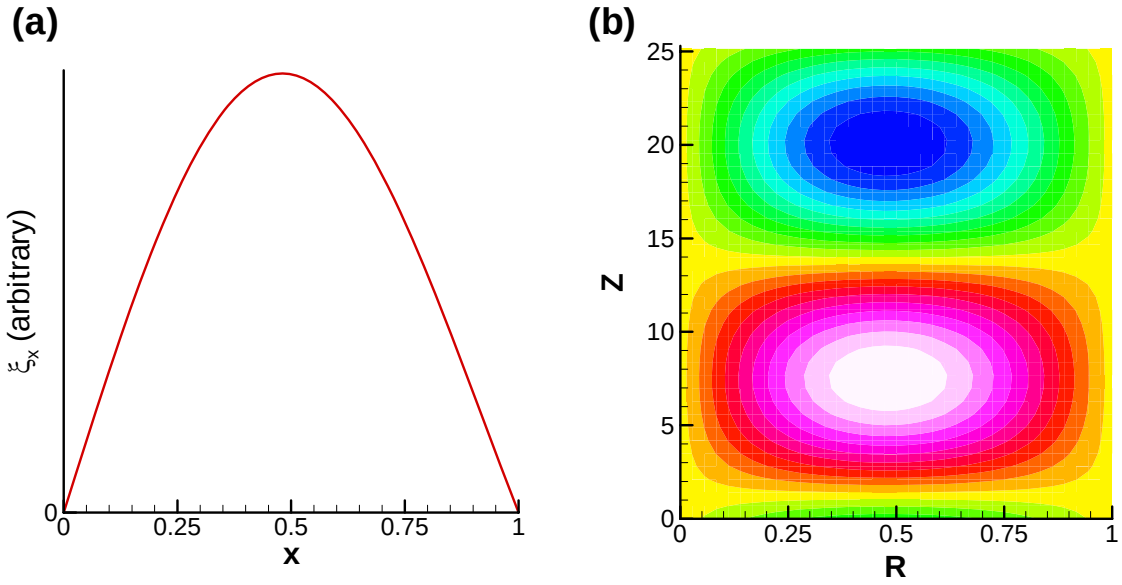


Figure 5. Radial displacement for the $k$=0.25, Φ=0.5 mode from eigenmode analysis (a) and contours of the radial component of velocity for the NIMROD computation with $r$-$z$ mesh (b).

grows with $\Gamma$=0.82. The growth-rate is only weakly dependent on the diffusivity for controlling magnetic divergence error; though, the level of divergence error responds. Increasing the spatial resolution is not effective. The same computation run with biquintic elements produces the unphysical mode at $\Gamma$=1.06. As shown in Fig. 6, the mode essentially appears in the nodes along the boundary only. Moreover, its growth-rate increases as time-step is decreased. With $\Delta t$=0.25, the numerical instability on the biquartic mesh grows at $\Gamma$=5.3.

Applying no-slip boundary conditions removes the unphysical mode. The result shown in Fig. 7 uses NIMROD's isotropic viscous damping (stress is proportional to the symmetrized rate-of-strain tensor), which automatically changes the boundary conditions from free-slip to no-slip. In this computation, the ratio of the viscous time to the Alfvén time is $2.5\times10^6$, and the resulting growth rate of 0.02428 is 5.5% below the free-slip growth rate. The mode is axisymmetric and resembles the eigenmode result of Fig. 5a. Reducing the viscosity many orders of magnitude changes the growth rate by less than 0.1%, so the no-slip condition is responsible for the difference between this mode and the eigenmode computation. This viscous damping itself is not affecting the result.

The specific cause of the unphysical wall mode has not been identified; though, some possibilities have been eliminated. If the problem were error in the linear combination of coefficients along the boundary, so that the effective normal direction used for the no-slip condition is not accurate, the error would decrease as the order of polynomials is increased. Instead, the numerical mode grows more rapidly with biquintic elements than with biquartic elements. The order of Gaussian quadrature has also been increased to check that contributions from the region near the boundary influence the finite element integrals accurately. This has little effect on the numerical mode. With the direct relation between the radial component of magnetic field and the radial component of displacement from Eq. (3a), one might expect that setting essential conditions on the normal components of both **V** and **B** overspecifies the boundary conditions. To check this, the code was modified to remove the essential condition on **B**. A computation performed with this modification shows the same unphysical result. Finally, one might wonder if a surface term is missing from the integration-by-parts performed on the linear ideal-MHD operator. [There is a surface term when the equilibrium magnetic field has a normal component at the wall and when the perturbed displacement has a normal component.] If this were the case, the error should decrease with decreasing time-step, but it increases. Nonetheless, to further test this hypothesis, we consider a computation with azimuthal mode number m=12 with the *r*-*z* mesh. This allows for the high poloidal wavenumber oscillations, like the result shown in Fig. 6a, and the integration-by-parts is the same regardless of geometry. While this produces an unresolved growing mode, its growth rate is low ($\Gamma\cong$0.016), and the eigenfunction is not just along the surface of the domain.

Returning to the free-slip biquintic computation, Fig. 8 shows that the unphysical mode compresses axial field and number density along the inner surface of the wall. However, the modeled response is apparently inadequate for compression of flow on small scales. This may result from the finite-element collocation of all fields. It leads to numerical properties that are similar to centered finite differences; numerical first-derivatives effectively have a null-space for oscillations with very large wavenumber. Why the mode appears at the boundary is also not known. The equilibrium pressure gradient is largest at the wall, which may be a contributing factor. The code may also be trying to generate a fast free-surface mode. However, a biquartic computation run with the Laplacian operator in the velocity advance and smaller time-steps

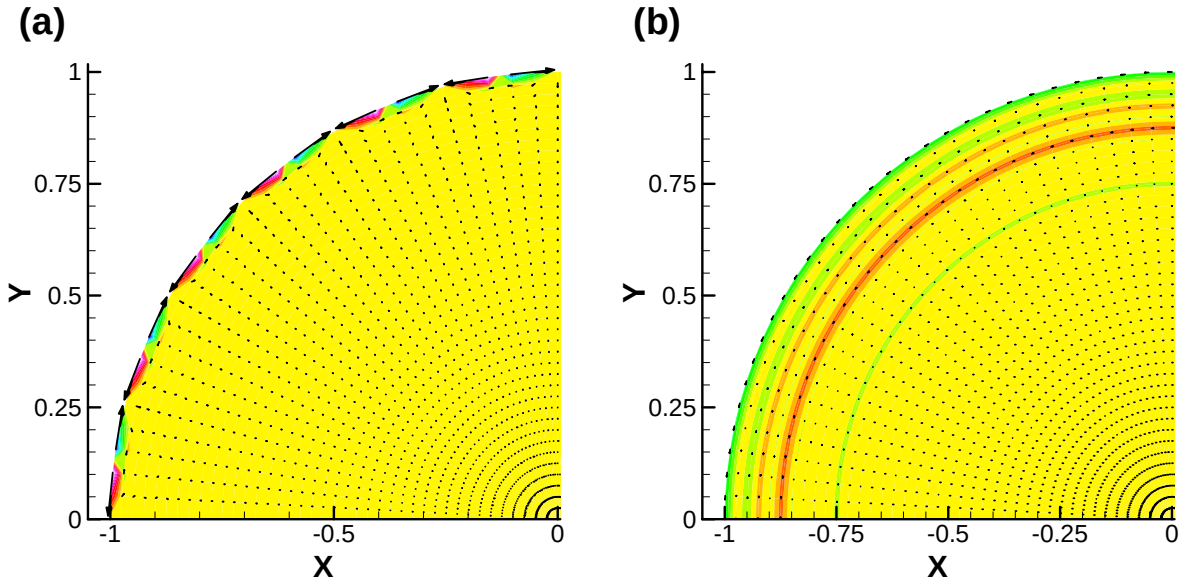


Figure 6. Real (a) and imaginary (b) parts of velocity for the numerical mode produced with the 8×24 (radial×azimuthal) mesh of biquintic elements for the inviscid $k$=0.25, $\Phi$=0.5 case. Vectors show components in the $r$-$\theta$ plane, and contours show the axial (out-of-plane) component. The color and vector-length scales are the same in the two plots, and only one quadrant of the domain is shown to make the vectors visible.

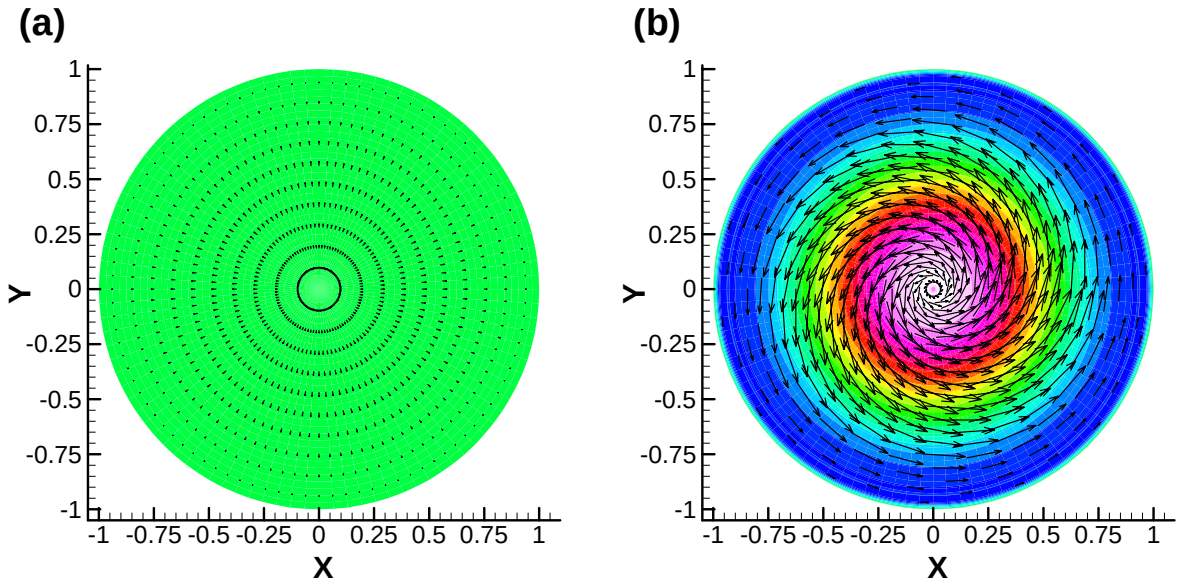


Figure 7. Real (a) and imaginary (b) parts of velocity for the physical mode produced with the 8×24 (radial×azimuthal) mesh of biquintic elements for the $k$=0.25, $\Phi$=0.5 case with moderate viscous damping and no-slip boundary conditions. The color and vector-length scales are the same in the two plots, but not all vectors are displayed.

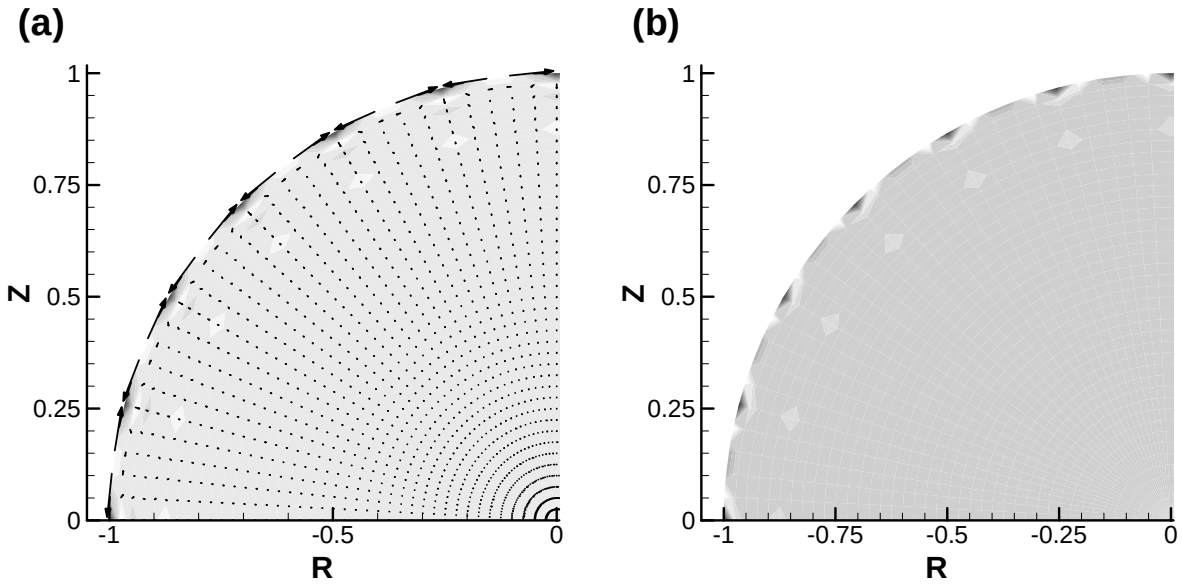


Figure 8. Contour plots of real $B_z$ (a) and real number density (b) for the computation shown in Fig. 6. Vectors in (a) redisplay the real part of velocity projected in the $r$-$\theta$ plane.

initially finds the axisymmetric mode at about the right growth-rate until volumetrically distributed high-wavenumber noise overtakes the physical mode. In this computation, the numerical instability grows at $\Gamma \cong 0.11$, which is faster than the physical mode but slower than the numerical instability with the standard velocity advance.

**4. Conclusions**

The results on ideal axisymmetric interchange reflect the project-wide experience with NIMROD simulations noted in the introduction. In many cases, such as the $\Phi=0$ calculations and the $\Phi\neq 0$ calculations on the $r$-$z$ mesh, the numerical results converge rapidly. However, other conditions lead to obvious numerical errors; a mode grows with $\Gamma\Delta t>1$ and/or has large oscillations on the finest scale supported by the basis functions. The no-slip boundary condition provides a patch for the $\Phi\neq 0$ calculations on the $r$-$\theta$ mesh, and it has been used with finite viscosity for years. However, this returns us to modifying the problem in order to have confidence in the numerical result.

The ideal-MHD system has a unique aspect for NIMROD calculations. Other than the semi-implicit operator, which is not dissipative, and the diffusion of magnetic divergence error, which should have little effect on the solenoidal part of the magnetic field, the system only has first-order derivatives acting on the solution fields. The effective null-space of the representation (described in Sect. 3.2) allows free energy in the physical configuration to drive instabilities without correct restoring responses. When physical dissipation is added, the highest-wavenumber oscillations are readily damped, and the effective null-space is removed. This argument is speculative, but it may also have bearing on the study of interchange performed in 2005, where sheared equilibria and no-slip boundary conditions find interchange somewhat below the Suydam criterion for instability.

If the speculation is correct, adapting techniques used to stabilize[3] spectral-element representations for fluid computations may improve NIMROD's performance. For example, finite-element computations of incompressible fluids often use a discontinuous representation of the pressure that has lower-order basis functions than the continuous basis functions used for the velocity components. While traditional fluid applications of finite elements have the pressure one order lower than velocity, Ref. 9 reports that spectral element methods are more successful with pressure two orders lower than velocity. For ideal-MHD, it may be logical use a lower-order discontinuous representation for pressure and the perpendicular component of magnetic field. Unfortunately, this would not allow us to add thermal conduction and electrical resistivity without adding surface terms between each element, because these terms apply higher-order differentiation. Using different continuous basis functions for different physical fields showed some promise in the 2005 study, but it is not satisfactory in all cases. Another possibility is the use of "bubble" nodes to add degrees of freedom to in-plane components of vector fields [10]. Future work will investigate these methods and extend the quantitative benchmarking to non-axisymmetric modes. The challenge will be to improve behavior on ideal interchange while retaining the high-order convergence properties of the present NIMROD implementation.

**References**


[1] R. Gruber and J. Rappaz, Finite Element Methods in Linear Ideal Magnetohydrodynamics, (Springer-Verlag, Berlin, 1985).

[2] L. M. Degtyarev and S. Yu. Medvedev, "Methods for numerical simulation of ideal MHD stability of axisymmetric plasmas," Comput. Phys. Commun. **43**, 29 (1986).

[3] C. R. Sovinec, A. H. Glasser, T. A. Gianakon, D. C. Barnes, R. A. Nebel, S. E. Kruger, D. D. Schnack, S. J. Plimpton, A. Tarditi, M. Ch u, and the NIMROD Team, "Nonlinear Magnetohydrodynamics Simulation using High-Order Finite Elements," J. Comput. Phys. **195**, 355 (2004).

[4] H. Lütjens and J. F. Luciani, "A class of basis functions for non-ideal magnetohydrodynamics computations," Comput. Phys. Commun. **95**, 47 (1996).

[5] W. Park, E. V. Belova, G. Y. Fu, X. Z. Tang, H. R. Strauss, and L. E. Sugiyama, "Plasma simulation studies using multilevel physics models," Phys. Plasmas **6**, 1796 (1999). Also see the M3DP User's Guide by J. Breslau and J. Chen, available from http://w3.pppl.gov/m3d/doc.html .

[6] G. Strang and G. J. Fix, An Analysis of the Finite Element Method, pp. 143-5 (Wellesley-Cambridge Press, Wellesley, Massachusetts, 1988).

[7] K. Hain and R. Lüst, "Zur Stabilität zylindersymmetrischer Plasmakonfigurationen mit Volumenströmen," Z. Naturforsch. A **13**, 936 (1958).

[8] J. P. Goedbloed and H. J. L. Hagebeuk, "Growth rates of instabilities of a diffuse linear pinch," Phys. Fluids **15**, 1090 (1972).

[9] M. O. Deville, P. F. Fischer, E. H. Mund, High-Order Methods for Incompressible Fluid Flow, pp. 240-2 (Cambridge University Press, Cambridge, 2002).

[10] C. Canuto and V. Van Kemenade, "Bubble-stabilized spectral methods for the incompressible Navier-Stokes equations," Comput. Methods Appl. Mech. Engrg. **135**, 35 (1996).


[3] The author's interpretation of this particular mathematical use of the term "stabilize" is to remove artificial null spaces from the numerical representation for a given differential system.

**Appendix**

Input for four of the NIMROD computations is provided below. The equilibria are generated from standard 1D profiles that are available in NIMSET. However, the standard profiles do not allow zero guide-field on axis, so a very small value is set through "be0" and the large value of "beta" is with respect to "be0," unlike the definition used in this report.

1. No guide-field, *r*-*z* mesh:

```
&grid_input
      gridshape='rect'
      periodicity='y-dir'
      geom='tor'
      mx=12
      my=24
      mxpie=1
      pieflag='rblock'
      nxbl=1
      nybl=1
      xmin=0.
      xmax=1.
      ymin=0.
      ymax=0.285625
      xo=0
      lin_nmax=0 /
&physics_input
      init_type="compr alf"
      eq_flow='none'
      advect='none'
      separate_pe=F
      continuity='fix profile'
      nx=3
      ny=4
      bamp=1.e-12
      ndens=3.80697e23
      elecd=1.e-10
      kin_visc=0.e-10
      dvac=10
      dexp=10
      ds_use='none'
      ohms='mhd'
      nonlinear=.false.
      beta=2.e12
      lamprof='pitprs'
      pit_0=1.e-6
      pres_2=-1.
      pres_4=0.
      lam0=1.e-10
      be0=1.e-6
      thetab=0.
      phib=0.25
      e_vertical=0
      loop_volt=0  /
&closure_input
      p_model='adiabat'
      k_pll=1.e5
      k_perp=10.
      ohm_heat=F
      visc_heat=F /
&numerical_input
      transfer_eq=F
      dtm=2.e-6
      poly_degree=3,
      dt_incr=1.07
```

```
      dt_change_frac=0.1
      ave_change_limit=1.e-2
      v_cfl=0.5
      fv_vdgv=0.54
      fb_vxb=0.54
      fp_vdgp=0.54
      fn_vdgn=0.54
      feta=1.
      fvsc=1.
      split_visc=.false.
      mhd_si_iso=0
      si_fac_mhd=1.5
      si_fac_pres=1.5
      si_fac_j0=1.
      si_fac_nl=2
      split_divb=.false.
      divbd=100.
      kdivb_2_limit=1.0
      ngr=2
      met_spl='iso'
      tmax=0.7
      cpu_tmax=12000,
      nstep=400 /
&solver_input
      solver='seq_slu'
      tol=1.e-9
      extrap_order=2
      maxit=500 /
&output_input
      nhist=1
      ihist=2
      jhist=2
      hist_binary=T
      ndump=250
      dump_over = 0
      dump_file='dump.00000' /


incha11l: short wavelength m=0 interchange without axial field.
Same as incha10l but uses the standard pitprs equilibrium; the
normalized pitch is equivalent to Bz/Btheta(a) if Bz is constant.

Alfven speed based on B(a) is 2.5e4, taua=4.e-5
```

2. No guide-field, *r*-$\theta$ mesh:

```
&grid_input
      gridshape='circ'
      geom='lin'
      mx=12
      my=24
      mxpie=1
      pieflag='rblock'
      nxbl=1
      nybl=1
      xmin=0.
      xmax=1.
      ymin=0.
      per_length=0.285625
      xo=0
      lin_nmax=2 /
&physics_input
      init_type="compr alf"
      eq_flow='none'
      advect='none'
```

```
      separate_pe=F
      continuity='fix profile'
      nx=3
      ny=0
      bamp=1.e-12
      ndens=3.80697e23
      elecd=1.e-10
      kin_visc=0.e-10
      dvac=10
      dexp=10
      ds_use='none'
      ohms='mhd'
      nonlinear=.false.
      beta=2.e12
      lamprof='pitprs'
      pit_0=1.e-6
      pit_2=0.
      pit_4=0.
      pres_2=-1.
      pres_4=0.
      lam0=1.e-10
      be0=1.e-6
      thetab=0.
      phib=0.25
      e_vertical=0
      loop_volt=0  /
&closure_input
      p_model='adiabat'
      k_pll=1.e5
      k_perp=10.
      ohm_heat=F
      visc_heat=F /
&numerical_input
      transfer_eq=F
      dtm=2.e-6
      poly_degree=3,
      dt_incr=1.07
      dt_change_frac=0.1
      ave_change_limit=1.e-2
      v_cfl=0.5
      fv_vdgv=0.54
      fb_vxb=0.54
      fp_vdgp=0.54
      fn_vdgn=0.54
      feta=1.
      fvsc=1.
      split_visc=.false.
      mhd_si_iso=0
      si_fac_mhd=1.5
      si_fac_pres=1.5
      si_fac_j0=1.
      si_fac_nl=2
      split_divb=.false.
      divbd=100.
      kdivb_2_limit=1.0
      ngr=2
      met_spl='iso'
      tmax=0.7
      cpu_tmax=12000,
      nstep=300 /
&solver_input
      solver='seq_slu'
      tol=1.e-9
      extrap_order=2
```

```
      maxit=500 /
&output_input
      nhist=1
      ihist=2
      jhist=2
      hist_binary=T
      ndump=2500
      dump_over = 0
      dump_file='dump.00000' /
```

```
inchb1l: short wavelength m=0 interchange without axial field.
Circular grid version of incha10l and uses default pitprs.
Alfven speed based on B(a) is 2.5e4, taua=4.e-5
```

3. Large guide-field, *r-z* mesh:

```
&grid_input
      gridshape='rect'
      periodicity='y-dir'
      geom='tor'
      mx=12
      my=12
      mxpie=1
      pieflag='rblock'
      nxbl=1
      nybl=1
      xmin=0.
      xmax=1.
      ymin=0.
      ymax=25.13274
      xo=0
      lin_nmax=0 /
&physics_input
      init_type="compr alf"
      eq_flow='none'
      advect='none'
      separate_pe=F
      continuity='fix profile'
      nx=1
      ny=2
      bamp=1.e-12
      ndens=3.80697e23
      elecd=1.e-10
      kin_visc=0.e-10
      dvac=10
      dexp=10
      ds_use='none'
      ohms='mhd'
      nonlinear=.false.
      beta=8.
      lamprof='pitprs'
      pit_0=0.5
      pres_2=-1.
      pres_4=0.
      lam0=1.e-10
      be0=0.5
      thetab=0.
      phib=0.25
      e_vertical=0
      loop_volt=0  /
&closure_input
      p_model='adiabat'
      k_pll=1.e5
```

```
      k_perp=10.
      ohm_heat=F
      visc_heat=F /
&numerical_input
      transfer_eq=F
      dtm=1.e-4
      poly_degree=3,
      dt_incr=1.07
      dt_change_frac=0.1
      ave_change_limit=1.e-2
      v_cfl=0.5
      fv_vdgv=0.54
      fb_vxb=0.54
      fp_vdgp=0.54
      fn_vdgn=0.54
      feta=1.
      fvsc=1.
      split_visc=.false.
      mhd_si_iso=0
      si_fac_mhd=1.
      si_fac_pres=1.
      si_fac_j0=1.
      si_fac_nl=2
      split_divb=.false.
      divbd=100.
      kdivb_2_limit=1.0
      ngr=2
      met_spl='iso'
      tmax=0.7
      cpu_tmax=12000,
      nstep=200 /
&solver_input
      solver='seq_slu'
      tol=1.e-9
      extrap_order=2
      maxit=500 /
&output_input
      nhist=1
      ihist=2
      jhist=2
      hist_binary=T
      ndump=50
      dump_over = 0
      dump_file='dump.00000' /


inchc2l: interchange with axial field
at constant pitch.
The normalized pitch is equivalent to Bz/Btheta(a) if Bz is constant.

Alfven speed based on B(a) is 2.5e4, taua=4.e-5
```

4. Large guide-field, $r$-$\theta$ mesh with viscosity:

```
&grid_input
      gridshape='circ'
      geom='lin'
      mx=8
      my=24
      mxpie=1
      pieflag='rblock'
      nxbl=1
      nybl=1
      xmin=0.
```

```
      xmax=1.
      ymin=0.
      per_length=25.13274
      xo=0
      lin_nmax=1 /
&physics_input
      init_type="compr alf"
      eq_flow='none'
      advect='none'
      separate_pe=F
      continuity='fix profile'
      nx=1
      ny=0
      bamp=1.e-12
      ndens=3.80697e23
      elecd=1.e-10
      iso_visc=1.e-2
      dvac=10
      dexp=10
      ds_use='none'
      ohms='mhd'
      nonlinear=.false.
      beta=8.
      lamprof='pitprs'
      pit_0=0.5
      pit_2=0.
      pit_4=0.
      pres_2=-1.
      pres_4=0.
      lam0=1.e-10
      be0=0.5
      thetab=0.
      phib=0.25
      e_vertical=0
      loop_volt=0  /
&closure_input
      p_model='adiabat'
      k_pll=1.e5
      k_perp=10.
      ohm_heat=F
      visc_heat=F /
&numerical_input
      transfer_eq=F
      dtm=1.e-4
      poly_degree=4,
      dt_incr=1.07
      dt_change_frac=0.1
      ave_change_limit=1.e-2
      v_cfl=0.5
      fv_vdgv=0.54
      fb_vxb=0.54
      fp_vdgp=0.54
      fn_vdgn=0.54
      feta=1.
      fvsc=0.5
      split_visc=.false.
      mhd_si_iso=0
      si_fac_mhd=1.
      si_fac_pres=1.
      si_fac_j0=1.
      si_fac_nl=2
      split_divb=.false.
      divbd=10.
      kdivb_2_limit=1.e6
```

```
      ngr=2
      met_spl='iso'
      tmax=0.7
      cpu_tmax=12000,
      nstep=100 /
&solver_input
      solver='seq_slu'
      tol=1.e-9
      extrap_order=2
      maxit=500 /
&output_input
      nhist=1
      ihist=2
      jhist=2
      hist_binary=T
      ndump=40
      dump_over = 0
      dump_file='dump.00000' /


inchd4l: interchange with axial field
at constant pitch.
pd=4
Alfven speed based on B(a) is 2.5e4, taua=4.e-5
```